

Deformed spin- $\frac{1}{2}$ square lattice in antiferromagnetic NaZnVOPO₄(HPO₄)S. Guchhait,¹ D. V. Ambika,² Qing-Ping Ding,² M. Uhlarz,³ Y. Furukawa,² A. A. Tsirlin,^{4,*} and R. Nath^{1,†}¹*School of Physics, Indian Institute of Science Education and Research, Thiruvananthapuram 695551, India*²*Ames Laboratory and Department of Physics and Astronomy, Iowa State University, Ames, Iowa 50011, USA*³*Dresden High Magnetic Field Laboratory (HLD-EMFL), Helmholtz-Zentrum Dresden-Rossendorf, 01328 Dresden, Germany*⁴*Felix Bloch Institute for Solid-State Physics, Leipzig University, 04103 Leipzig, Germany*

(Received 15 June 2022; revised 17 July 2022; accepted 18 July 2022; published 28 July 2022)

We report the structural and magnetic properties of a new spin-1/2 antiferromagnet NaZnVOPO₄(HPO₄) studied via x-ray diffraction, magnetic susceptibility, high-field magnetization, specific heat, and ³¹P nuclear magnetic resonance (NMR) measurements, as well as density-functional band-structure calculations. While thermodynamic properties of this compound are well described by the J_1 - J_2 square-lattice model, *ab initio* calculations suggest a significant deformation of the spin lattice. From fits to the magnetic susceptibility we determine the averaged nearest-neighbor and second-neighbor exchange couplings of $\bar{J}_1 \simeq -1.3$ K and $\bar{J}_2 \simeq 5.6$ K, respectively, resulting in the effective frustration ratio $\alpha = \bar{J}_2/\bar{J}_1 \simeq -4.3$ that implies columnar antiferromagnetic order as the ground state. Experimental saturation field of 15.3 T is consistent with these estimates if 20% spatial anisotropy in J_1 is taken into account. Specific heat data signal the onset of a magnetic long-range order at $T_N \simeq 2.1$ K, which is further supported by a sharp peak in the NMR spin-lattice relaxation rate. The NMR spectra mark the superposition of two P lines due to two nonequivalent P sites where the broad line with the strong hyperfine coupling and short T_1 is identified as the P(1) site located within the magnetic planes, while the narrow line with the weak hyperfine coupling and long T_1 is designated as the P(2) site located between the planes.

DOI: [10.1103/PhysRevB.106.024426](https://doi.org/10.1103/PhysRevB.106.024426)

I. INTRODUCTION

Low-dimensional spin systems augmented with strong frustration reveal suppression of a conventional magnetic order and may lead to a quantum disordered ground state like quantum spin liquid (QSL) [1]. Two-dimensional (2D) spin-1/2 frustrated square-lattice (FSL) is a well-known example where frustration appears because of the competition between nearest-neighbor (NN, J_1) and next-nearest-neighbor (NNN, J_2) exchange interactions along the edges and diagonals of a square, respectively (J_1 - J_2 model). Theoretical studies have determined a global phase diagram with different ground states depending on the sign and relative strength of the exchange couplings ($\alpha = J_2/J_1$) [2,3]. Assuming antiferromagnetic J_2 , ferromagnetic (FM) state is expected for $-0.5 < \alpha < 0$, Néel antiferromagnetic state (NAF) state is expected for $0 < \alpha < 0.5$, and columnar antiferromagnetic (CAF) state is expected for $|\alpha| > 0.5$ on the classical level. Adding quantum corrections can stabilize different disordered phases at the phase boundaries, leading to novel order parameters or the quantum critical regimes. For instance, QSL [4–6], plaquette valence-bond solid (PVBS) [7,8] or columnar valence-bond solid (CVBS) [9] states are expected around $\alpha \simeq 0.5$, while a spin nematic phase is predicted for $\alpha \simeq -0.5$ in the phase diagram [10].

In the recent past, a handful number of Cu²⁺ ($3d^9$), V⁴⁺ ($3d^1$), and Mo⁵⁺ ($4d^1$) based spin-1/2 FSL magnets have been studied as J_1 - J_2 model compounds. The vanadates are the most celebrated ones and include Li₂VOXO₄ ($X = \text{Si, Ge}$) with $J_1, J_2 > 0$ and $J_2 \gg J_1$ [11,12], along with V⁴⁺ phosphates that typically show $J_1 < 0$ and $J_2 > 0$, also resulting in the CAF ground state [13–18]. A few other vanadates, such as Zn₂VO(PO₄)₂ [19], VOMoO₄ [20–22], and PbVO₃ [23], feature $J_1 \gg J_2$ and lie in the NAF region of the phase diagram. A further variability becomes possible with Cu²⁺ as well as $4d$ Mo⁵⁺ compounds that span both $J_2 \gg J_1$ and $J_2 \ll J_1$ limits [24–32]. Unfortunately, none of these compounds fall in the quantum critical regimes of the phase diagram around $|\alpha| = 1/2$. Moreover, some of them show intricate deformations of the magnetic square lattice, because the underlying crystal symmetry is lower than tetragonal [33]. This deformation was verified experimentally in several V⁴⁺ phosphates, including Pb₂VO(PO₄)₂ [34], SrZnVO(PO₄)₂ [35], and BaCdVO(PO₄)₂ [36]. Each of them showed an interesting pre-saturation phase [35,37–40], which is reminiscent of the nematic phase of the J_1 - J_2 model [10], but deviations from the ideal square lattice put into question the applicability of this theoretical scenario, and alternative interpretations were indeed proposed recently [41,42].

In this context, finding V⁴⁺ square-lattice compounds with different magnitudes of the deformation is important. Here, we report low-temperature magnetic behavior of the hitherto unexplored NaZnVOPO₄(HPO₄) as a spin-1/2 square-lattice candidate with a different spacer separating the magnetic

*altsirlin@gmail.com

†rnath@iisertvm.ac.in

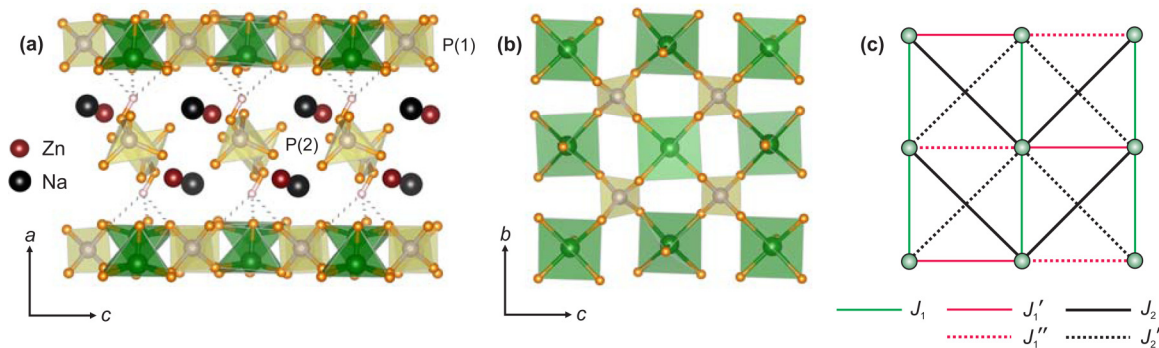


FIG. 1. (a) Crystal structure of $\text{NaZnVOPO}_4(\text{HPO}_4)$ with the hydrogen position and hydrogen bonds (dashed lines) determined in this work. (b) Magnetic $[\text{VOPO}_4]$ layer with the square-lattice-like arrangement of the V^{4+} ions. (c) Deformed square lattice with five nonequivalent interactions. VESTA software [43] was used for crystal structure visualization.

layers and, potentially, a different regime of exchange couplings compared to the widely studied $AA'\text{VO}(\text{PO}_4)_2$ phosphates ($AA' = \text{Pb}_2, \text{SrZn}, \text{BaCd}$). The monoclinic crystal structure of $\text{NaZnVOPO}_4(\text{HPO}_4)$ features V^{4+} ions in the square-pyramidal coordination. They are joined into layers via $\text{P}(1)\text{O}_4$ tetrahedra (Fig. 1), while the interlayer space is filled with the Na^+ and Zn^{2+} ions, as well as the $\text{P}(2)\text{O}_4$ tetrahedra that represent the HPO_4 groups.

II. METHODS

Pale-blue colored powder of the titled compound was synthesized by the conventional hydrothermal method. 0.150 g Na_2CO_3 (Aldrich, 99.995%), 0.154 g V_2O_5 (Aldrich, 99.99%), and 0.115 g Zn (Aldrich, 99%) powders were mixed with 5 ml of a 1.5 M aqueous solution of H_3PO_4 , sealed in a 23 ml teflon lined bomb, and heated at 240°C for 8 days followed by slow cooling ($10^\circ\text{C}/\text{hour}$) to room temperature. The obtained blue color product was washed carefully with distilled water and dried in an oven maintained at 100°C for 24 hours. To check the phase purity of the compound, powder x-ray diffraction (XRD) experiment was performed using a PANalytical powder diffractometer with $\text{Cu } K_\alpha$ radiation ($\lambda_{\text{avg}} \simeq 1.5418 \text{ \AA}$) at room temperature. We have also performed temperature-dependent powder XRD measurements on the phase-pure powder sample in the temperature range $15 \text{ K} \leq T \leq 300 \text{ K}$, using a low-temperature attachment (Oxford PheniX) to the x-ray diffractometer. Le Bail fit of the powder XRD patterns was performed using the FULLPROF software package [44], taking the initial structural parameters from the previous report [45].

Temperature variation of magnetization (M) was measured in the temperature range 1.8–350 K in different magnetic fields (H) using a SQUID magnetometer (MPMS3, Quantum Design). The isothermal magnetization was measured at $T = 1.8 \text{ K}$ from 0 to 7 T. The high-field magnetization measurement was performed at $T = 1.4 \text{ K}$ in pulsed magnetic fields up to 30 T using the facility at the Dresden High Magnetic Field Laboratory [46,47]. The temperature-dependent specific heat of this sample was measured on a sintered pellet in a large temperature range ($0.5 \text{ K} \leq T \leq 200 \text{ K}$) using the Physical Property Measurement System (PPMS, Quantum Design) and adopting the thermal relaxation technique. For measurements below 2 K, ^3He attachment to the PPMS was used.

The nuclear magnetic resonance (NMR) measurements were carried out on the ^{31}P nuclei (gyromagnetic ratio $\frac{\gamma_N}{2\pi} = 17.237 \text{ MHz/T}$ and nuclear spin $I = 1/2$) in the temperature range $1.8 \text{ K} \leq T \leq 250 \text{ K}$. The NMR spectra at different temperatures were obtained by varying the magnetic field at a constant frequency of 121 MHz. The spin-lattice relaxation rate ($1/T_1$) was measured by the single saturation pulse method at two frequencies (30.2 and 121 MHz). The temperature-dependent NMR shift, $K(T) = [H_{\text{ref}}/H(T) - 1]$, was calculated from the resonance field of the sample H with respect to the resonance field of a nonmagnetic reference sample (H_{ref}).

Magnetic couplings were determined by density-functional-theory (DFT) band-structure calculations performed in the FPLO code [48] using experimental structural parameters from Ref. [45], except the hydrogen position that was optimized as further explained in Sec. III E. The Perdew-Burke-Ernzerhof (PBE) approximation for the exchange-correlation potential was employed [49]. We used superexchange theory in the vein of Kugel-Khomskii model [50,51], as well as the mapping approach [52,53] based on total energies of collinear spin configurations obtained from DFT + U calculations with the on-site Coulomb repulsion $U_d = 4 \text{ eV}$, Hund's coupling $J_d = 1 \text{ eV}$, and double-counting correction in the atomic limit [54].

Experimental thermodynamic properties were modeled by high-temperature series expansion (HTSE) for the J_1 - J_2 spin-1/2 square lattice [55] as well as full diagonalization (FD) for the 4×4 finite lattice with periodic boundary conditions. Additionally, quantum Monte Carlo (QMC) simulations were performed for the nonfrustrated spin-1/2 square lattice using directed loop algorithm [56] in the stochastic series expansion (SSE) [57] representation. QMC simulations were performed for 16×16 finite lattices with periodic boundary conditions, using 4×10^4 sweeps and 4×10^3 thermalization sweeps. The ALPS package [58] was used for both FD and QMC.

III. RESULTS

A. X-ray diffraction

The powder XRD patterns of $\text{NaZnVOPO}_4(\text{HPO}_4)$ are analyzed by Le Bail fits. Figure 2 presents the data at two end temperatures ($T = 300$ and 15 K). The entire XRD pattern down to 15 K could be indexed using the monoclinic

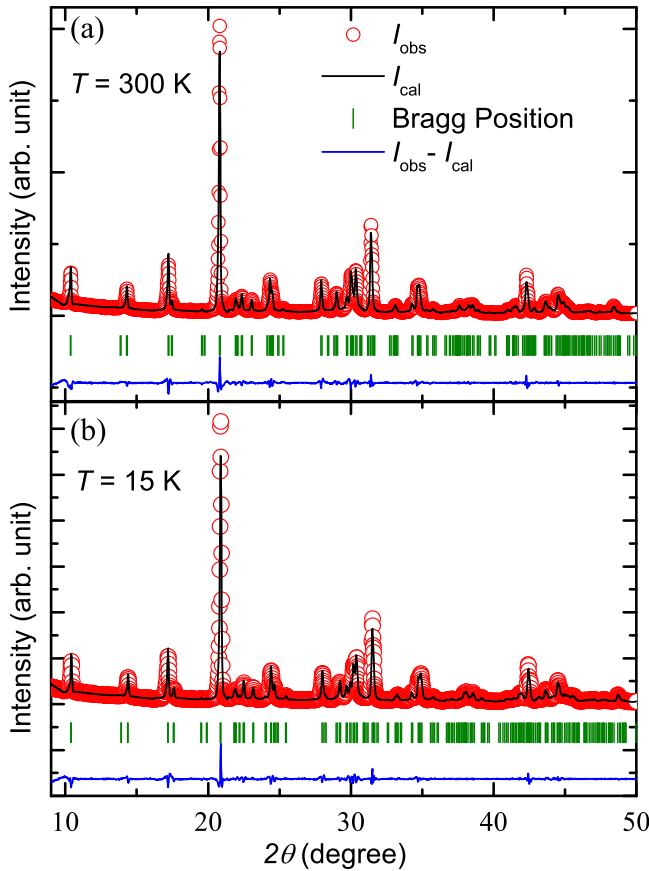


FIG. 2. Powder XRD patterns (open circles) at (a) $T = 300$ and (b) 15 K. The solid line is the Le Bail fit, the vertical bars mark the expected Bragg peak positions, and the lower solid line corresponds to the difference between the observed and calculated intensities. The goodness-of-fit is achieved to be $\chi^2 \sim 5.4$ and ~ 6.2 for $T = 300$ and 15 K, respectively.

crystal structure with the space group $P2_1/c$. Neither structural transition nor lattice distortion are observed down to 15 K. The refined lattice parameters and unit cell volume (V_{cell}) are $a = 8.5418(4)$ Å, $b = 8.9937(5)$ Å, $c = 9.0765(5)$ Å, $\beta = 91.186(3)^\circ$, and $V_{\text{cell}} \simeq 696.46$ Å³ and $a = 8.5190(2)$ Å, $b = 8.9281(4)$ Å, $c = 9.1029(4)$ Å, $\beta = 92.013(5)^\circ$, and $V_{\text{cell}} \simeq 691.73$ Å³ for $T = 300$ and 15 K, respectively. The obtained lattice parameters at room temperature are in close agreement with the values reported earlier [45]. The temperature dependence of the lattice parameters (a , b , c , and β) and V_{cell} are presented in Fig. 3. The lattice constants a and b are found to decrease in a systematic way with decreasing temperature while c and monoclinic angle β increase with decreasing temperature and then reach a plateau. These lead to an overall thermal contraction of the V_{cell} with temperature.

The variation of V_{cell} with temperature can be expressed in terms of the internal energy [$U(T)$] of the system [59,60]:

$$V_{\text{cell}}(T) = \frac{\gamma U(T)}{K_0} + V_0. \quad (1)$$

Here, V_0 is the unit cell volume at $T = 0$ K, γ is the Grüneisen parameter, and K_0 is the bulk modulus of the system.

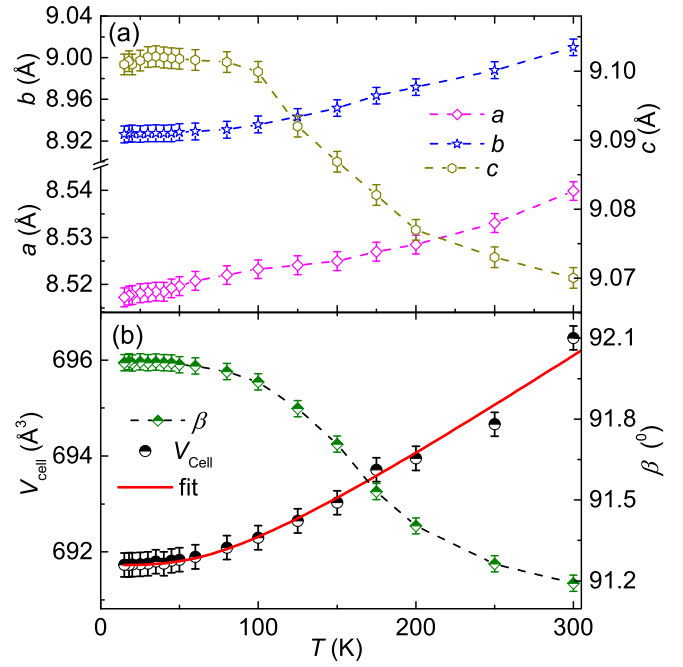


FIG. 3. (a) Lattice constants (a , b , and c) as a function of temperature. (b) Monoclinic angle (β) along with the unit cell volume (V_{cell}) are plotted as a function of temperature from 15 to 300 K. The solid line represents the fit of V_{cell} using Eq. (1).

According to the Debye model, $U(T)$ can be written as

$$U(T) = 9Nk_B T \left(\frac{T}{\theta_D} \right)^3 \int_0^{\theta_D/T} \frac{x^3}{(e^x - 1)} dx, \quad (2)$$

where N is the total number of atoms per unit cell, k_B is the Boltzmann constant, and θ_D is the Debye temperature [61]. The variable x inside the integration stands for the quantity $\frac{\hbar\omega}{k_B T}$ with phonon frequency ω and Planck constant \hbar . Here, $\theta_D = \frac{\hbar\omega_D}{k_B}$ and ω_D is the upper limit of ω . The best fit of the $V_{\text{cell}}(T)$ data using Eq. (1) [solid line in Fig. 3(b)] yields the parameters: $\theta_D = 312(8)$ K, $V_0 = 691.7(5)$ Å³, and $\frac{\gamma}{K_0} \simeq 8.84 \times 10^{-12}$ Pa⁻¹.

B. Magnetization

The magnetic susceptibility [$\chi(T) \equiv M/H$] of $\text{NaNzVOPO}_4(\text{HPO}_4)$ measured in an applied field of $H = 0.5$ T is shown in Fig. 4(a). In the high-temperature region, $\chi(T)$ follows a typical Curie-Weiss (CW) behavior and shows a rounded maximum at $T_\chi^{\text{max}} \simeq 4.6$ K. Such a maximum represents the short-range AFM order in the low-dimensional spin systems. Below about 2.6 K, a small upturn is likely due to paramagnetic impurities and/or defects present in the powder sample. No trace of magnetic long-range-order (LRO) is detected down to 2 K. We have also measured $\chi(T)$ in different applied fields [inset of Fig. 4(b)] but no obvious features associated with magnetic LRO is found, except the suppression of a broad maximum towards low temperatures.

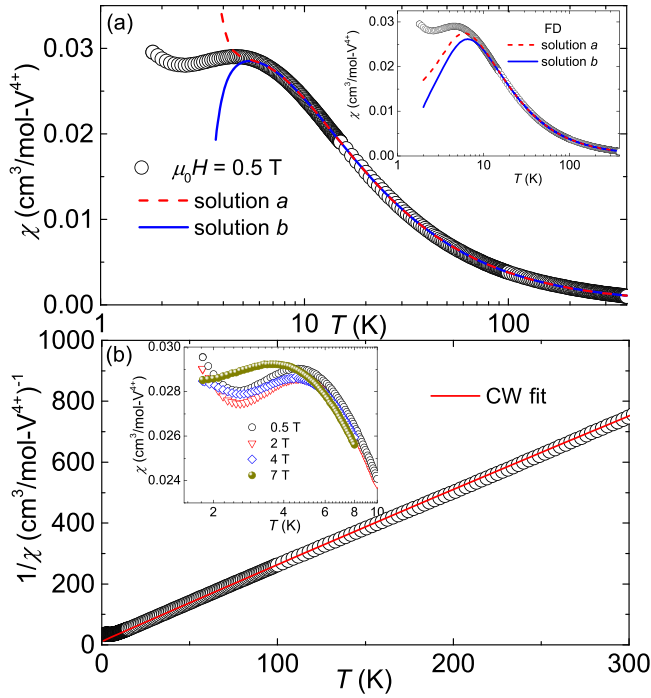


FIG. 4. (a) $\chi(T)$ measured in the magnetic field of $H = 0.5$ T. The lines (solid and dashed) are the HTSE fits using the isotropic spin-1/2 FSL model, with two different solutions (solutions *a* and solution *b*). (Inset) The simulated $\chi(T)$ using the FD method taking the J_1 and J_2 values from solutions *a* and *b*, respectively. (b) $1/\chi$ vs T . The red solid line is the CW fit. (Inset) $\chi(T)$ in the low- T region measured in different fields.

The inverse susceptibility, $1/\chi(T)$, is shown in Fig. 4(b). In the paramagnetic regime, $1/\chi(T)$ was fitted by the CW law

$$\chi(T) = \chi_0 + \frac{C}{T - \theta_{CW}}, \quad (3)$$

where the first term (χ_0) represents the combination of temperature-independent diamagnetic and Van Vleck paramagnetic susceptibilities. The second term is the CW law where C is the Curie constant and θ_{CW} is the CW temperature. The fit above 25 K returns the parameters: $\chi_0 \simeq 4.26 \times 10^{-5} \text{ cm}^3 \text{ mol}^{-1}/\text{V}^{4+}$, $C \simeq 0.393 \text{ cm}^3 \text{ K mol}^{-1}/\text{V}^{4+}$, and $\theta_{CW} = -4.3(3) \text{ K}$. Using the value of C , the effective moment is calculated to be $\mu_{\text{eff}} [= (3k_B C/N_A \mu_B^2)^{1/2}]$, where N_A is the Avogadro number and μ_B is the Bohr magneton] $\simeq 1.77 \mu_B/\text{V}^{4+}$. This value of μ_{eff} is close to the actual value $1.73 \mu_B$ for a spin-1/2 transition-metal ion with $g = 2$. The negative value of θ_{CW} indicates the dominant AFM exchange coupling between the V^{4+} ions. The core diamagnetic susceptibility (χ_{core}) of the compound caused by the core orbital electrons was calculated to be $-1.37 \times 10^{-4} \text{ cm}^3/\text{mol}$ by adding the χ_{core} of Na^+ , Zn^{2+} , V^{4+} , P^{5+} , and O^{2-} ions [62]. The Van-Vleck paramagnetic susceptibility (χ_{vv}) was calculated to be $\sim 1.8 \times 10^{-4} \text{ cm}^3/\text{mol}$ by subtracting χ_{core} from χ_0 , which is very close to the value reported for other V^{4+} based compounds [63].

As evident from the structural data (Fig. 1), the system deviates from the isotropic square lattice. This spatial anisotropy is mainly due to five nonequivalent exchange couplings, three

between nearest neighbors (J_1 , J'_1 , and J''_1) and two between next-nearest neighbors (J_2 and J'_2). Previous studies suggest that this anisotropy has only a minor effect on thermodynamic properties at higher temperatures [33]. Therefore fits with the isotropic $J_1 - J_2$ model return averaged values of the NN and NNN couplings, $\bar{J}_1 = (2J_1 + J'_1 + J''_1)/4$ and $\bar{J}_2 = (J_2 + J'_2)/2$, respectively. We fitted the data with

$$\chi(T) = \chi_0 + \chi_{\text{spin}}(T) \quad (4)$$

using the temperature-independent term (χ_0) and the ninth-order HTSE [$\chi_{\text{spin}}(T)$],

$$\chi_{\text{spin}}(T) = \frac{N_A g^2 \mu_B^2}{k_B T} \sum_n \left(\frac{\bar{J}_1}{k_B T} \right)^n \sum_m c_{mn} \left(\frac{\bar{J}_2}{\bar{J}_1} \right)^m. \quad (5)$$

The values of the coefficients c_{mn} are taken from Ref. [55]. Our fit for $T \geq 7 \text{ K}$ yields two solutions: solution *a* with $\chi_0 \simeq 6 \times 10^{-5} \text{ cm}^3 \text{ mol}^{-1}/\text{V}^{4+}$, $g \simeq 2.04$, $\bar{J}_1 \simeq 5.18 \text{ K}$, $\bar{J}_2 \simeq -0.66 \text{ K}$ and solution *b* with $\chi_0 \simeq 6.6 \times 10^{-5} \text{ cm}^3 \text{ mol}^{-1}/\text{V}^{4+}$, $g \simeq 2.04$, $\bar{J}_1 \simeq -1.28 \text{ K}$, $\bar{J}_2 \simeq 5.59 \text{ K}$.

The main difficulty of the HTSE fit is choosing the appropriate T -range. The convergence of the HTSE depends on the \bar{J}_2/\bar{J}_1 ratio, hence the lower limit of the fitting range (T_{min}) should be chosen with caution depending on the results of the fit [15]. For a precise estimation of the J values, we varied the lower limit of the fitting T -range (T_{min}) between 5 and 9 K and estimated the exchange couplings for both the solutions. Figures 5(a) and 5(b) present the variation of \bar{J}_1 and \bar{J}_2 with T_{min} for the solutions-*a* and *b*, respectively. To check the convergence of the HTSE, we calculated the ratio of the ninth-order term to the total susceptibility [$\chi_9(T)/\chi_{\text{total}}(T)$] using the parameters obtained from HTSE fits with a different T_{min} . Both solutions are stable above 7 K. We also performed the FD simulations of $\chi(T)$ using the values of χ_0 , g , \bar{J}_1 , and \bar{J}_2 and found a good agreement with the experimental data [inset of Fig. 4(a)]. From the dependence on T_{min} we estimate the error bar less than 0.1 K for the exchange couplings \bar{J}_1 and \bar{J}_2 . Discriminating between the solutions-*a* and *b* may be possible using measurements of the saturation field [47]. The M versus H data measured up to 25 T in pulsed magnetic fields at $T = 1.4 \text{ K}$ are shown in Fig. 6. We have scaled the high-field data with respect to the magnetic isotherm at $T = 1.8 \text{ K}$ measured up to 7 T using a SQUID magnetometer. M increases linearly with H in the low-field region, shows a positive curvature in the intermediate fields, and then saturates at around $H_S \simeq 15.3 \text{ T}$. The positive curvature is typical for low-dimensional and frustrated spin systems [64].

Saturation field of an FSL magnet depends on the type of magnetic order. In the NAF case (solution *a*), $H_S = 4\bar{J}_1 k_B / (g\mu_B) \simeq 15.1 \text{ T}$ in good agreement with the experiment. On the other hand, in the CAF case $H_S = (\bar{J}_1 + 2\bar{J}_2) 2k_B / (g\mu_B)$ where \bar{J}_1 is the weaker of the couplings J_1 and $(J'_1 + J''_1)/2$. In the CAF state, spins align antiferromagnetically along the direction of this coupling and ferromagnetically along the orthogonal direction. Therefore only the weaker coupling enters the saturation field. Using $\bar{J}_1 = \bar{J}_1$ leads to $H_S^{\text{CAF}} \simeq 14.45 \text{ T}$ for the solution-*b*, lower than in the experiment. On the other hand, the actual value of \bar{J}_1 can be reduced owing to the deformation of the square lattice. Assuming 20% spatial anisotropy in the NN couplings

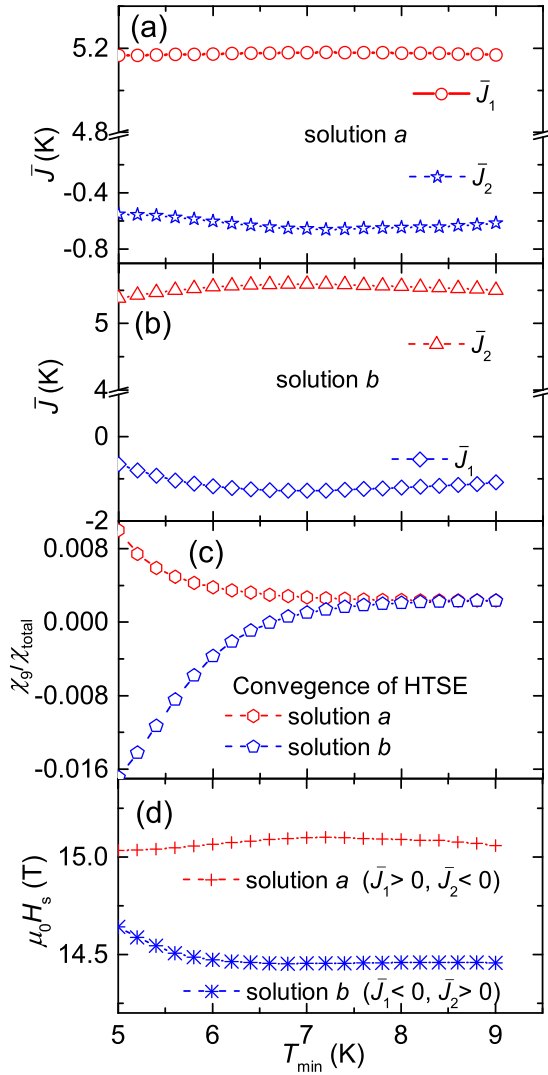


FIG. 5. Results of the $\chi(T)$ fit using HTSE for isotropic spin-1/2 FSL model by varying the minimum temperature of the fitting range (T_{\min}). [(a) and (b)] Averaged exchange interactions (\bar{J}_1 and \bar{J}_2) vs T_{\min} for the solutions *a* and *b*, respectively. (c) Convergence test of the HTSE fit for both solutions, $\chi_9(T)/\chi_{\text{total}}(T)$ vs T_{\min} . (d) Saturation fields for the solutions *a* and *b* vs T_{\min} .

($\mathcal{J}_1 = 0.8\bar{J}_1$) according to the DFT results (Sec. III E), we arrive at $H_S^{\text{CAF}} \simeq 15.15$ T, which is on par with the result for the solution *a* and also matches the experimental value.

Interestingly, the magnetization curve can be also well described by the simple NN square-lattice model with an effective coupling $J_{\text{eff}} = 5.1$ K (Fig. 6), which is in good agreement with the leading exchange couplings extracted from the HTSE fits.

C. Specific Heat

In Fig. 7(a), we have plotted the temperature-dependent specific heat [$C_p(T)$] measured from 0.5 to 140 K in zero applied field. It decreases systematically with temperature and passes through a broad maximum at $T_C^{\text{max}} \simeq 3.7$ K, typical for low-dimensional oxides. An anomalous behavior was observed in a narrow temperature range $T_N = 2\text{--}2.2$ K where we

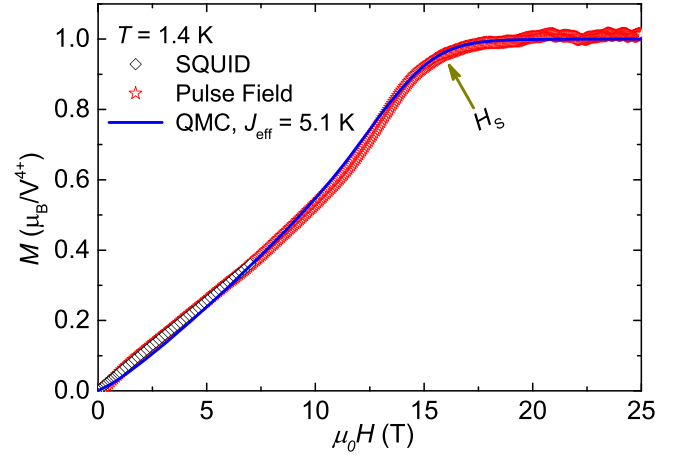


FIG. 6. Magnetization (M) vs field (H) at $T = 1.4$ K measured using pulse magnetic field and scaled with respect to the SQUID data. The solid line represents the QMC simulation, assuming the spatially isotropic nonfrustrated spin-1/2 square-lattice model with $J_{\text{eff}} = 5.1$ K. The arrow indicates the position of the saturation field (H_s).

couldn't stabilize the temperature. This is a possible indication of the onset of a magnetic LRO.

In a magnetic insulator, the total specific heat $C_p(T)$ is the sum of two main contributions: one is the phonon/lattice contribution [$C_{\text{ph}}(T)$], which dominates in the high-temperature region, and another one is the magnetic contribution [$C_{\text{mag}}(T)$], which dominates in the low-temperature region depending upon the strength of the exchange coupling. In order to bring out the magnetic part of the specific heat, we first quantified the lattice contribution and then subtracted it from the total specific heat. We simulated the high-temperature $C_{\text{ph}}(T)$ data taking into account the sum of one Debye [$C_{\text{D}}(T)$] and three Einstein [$C_{\text{E}}(T)$] terms, i.e., $C_{\text{ph}}(T) = C_{\text{D}}(T) + \sum_{i=1}^3 C_{\text{E}i}(T)$. The Debye and Einstein terms are expressed as

$$C_{\text{D}}(T) = 9n_{\text{D}}R \left(\frac{T}{\theta_{\text{D}}} \right)^3 \int_0^{\theta_{\text{D}}/T} \frac{x^4 e^x}{(e^x - 1)^2} dx \quad (6)$$

and

$$C_{\text{E}i}(T) = 3n_{\text{E}i}R \left(\frac{\theta_{\text{E}i}}{T} \right)^2 \frac{e^{(\theta_{\text{E}i}/T)}}{[e^{(\theta_{\text{E}i}/T)} - 1]^2}. \quad (7)$$

Here, the Einstein temperatures $\theta_{\text{E}i} = \frac{\hbar\omega_{\text{E}i}}{k_{\text{B}}}$, $\omega_{\text{E}i}$ are the respective Einstein frequencies, and R denotes the universal gas constant. The values of n_{D} and $n_{\text{E}i}$ are chosen in such a way that the sum $n_{\text{D}} + \sum_{i=1}^3 n_{\text{E}i}$ matches with the total number of atoms per formula unit. The best fit of the C_p data in the high-temperature regime using one Debye and three Einstein branches yields the characteristic temperatures: $\theta_{\text{D}} \simeq 122$ K, $\theta_{\text{E}1} \simeq 307$ K, $\theta_{\text{E}2} \simeq 850$ K, and $\theta_{\text{E}3} \simeq 161$ K with $n_{\text{D}} = 1$, $n_{\text{E}1} = 5$, $n_{\text{E}2} = 7$, and $n_{\text{E}3} = 2$, respectively [65]. The red solid line in Fig. 7(a) is the total phononic contribution to the specific heat (C_{ph}) extrapolated down to low temperature, while the dashed and dash-dotted lines are the Einstein and Debye contributions, respectively. The average of θ_{D} and θ_{E}

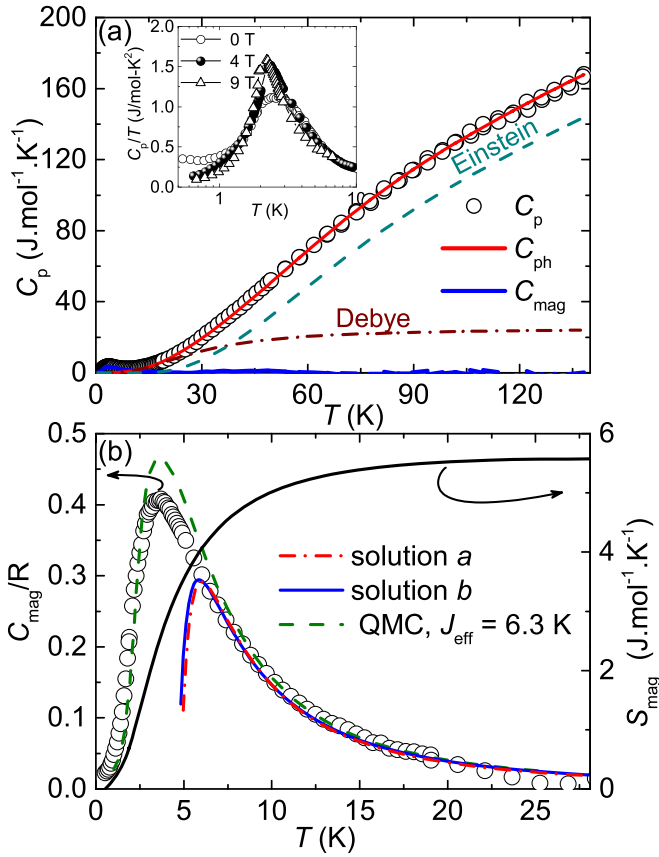


FIG. 7. (a) Variation of C_p with temperature in the absence of magnetic field. The red solid line represents the simulated phonon contribution (C_{ph}) taking into account the Debye (dash-dotted line) and Einstein (dashed line) terms. (Inset) C_p/T vs T at low temperatures and in different applied fields. The blue solid line is the magnetic contribution (C_{mag}). (b) C_{mag}/R vs T (left y axis). The solid line represents the change in the magnetic entropy, S_{mag} vs T (right y axis). The red (dash-dotted) and blue (solid) lines are the HTSE fits corresponding to the two solutions, respectively. The green (dashed) line is the QMC simulation for an isotropic nonfrustrated spin-1/2 square lattice model with $J_{eff} = 6.3$ K.

values reasonably matches θ_D estimated from the V_{cell} versus T analysis.

C_{mag} estimated after subtracting C_{ph} from C_p is plotted in Fig. 7(b) as a function of temperature. The pronounced broad maximum at $T_C^{max} \simeq 3.7$ K mimics short-range antiferromagnetic correlations. The change in magnetic entropy [$S_{mag}(T)$] is obtained by integrating C_{mag}/T over temperature. It saturates to a value of ~ 5.6 J mol $^{-1}$ K $^{-1}$ at around $T \simeq 25$ K, which is close to the expected value $R \ln 2 = 5.76$ J mol $^{-1}$ K $^{-1}$ for a two-level (spin-1/2) system, thus justifying our subtraction procedure and the evaluation of C_{mag} .

The magnetic LRO is highlighted by plotting C_p/T versus T in the inset of Fig. 7(a) in different applied fields. While the anomaly associated with the magnetic LRO is not pronounced in the zero-field data, the peak at $T_N \simeq 2.1$ K becomes more pronounced with increasing the field. This is due to the transfer of entropy from the broad maximum to the transition anomaly. Surprisingly, no visible shift in T_N is

perceived even with the field change of 9 T, indication of a robust AFM transition.

One can estimate the exchange couplings by analyzing $C_{mag}(T)$ using the HTSE of a spin-1/2 FSL model [55],

$$\frac{C_{mag}(T)}{R} = \frac{\bar{J}_1}{k_B T} \sum_n (-n) \left(\frac{\bar{J}_1}{k_B T} \right)^n \sum_m e^{m n} \left(\frac{\bar{J}_2}{\bar{J}_1} \right)^m. \quad (8)$$

We have fitted the $C_{mag}(T)/R$ data at $T > 6$ K [see Fig. 7(b)] and arrived at two solutions that strongly resemble the two solutions from the susceptibility fit: solution a ($\bar{J}_1/k_B \simeq 5.9$ K, $\bar{J}_2/k_B \simeq -0.2$ K) and solution b ($\bar{J}_1/k_B \simeq -1.6$ K, $\bar{J}_2/k_B \simeq 6.1$ K). Alternatively, we can compare our experimental data with the QMC simulation for the nonfrustrated square-lattice model [see Fig. 7(b)]. The position of the maximum in C_{mag} is reproduced with $J_{eff} = 6.3$ K, which is notably higher than in the $M(H)$ fit (Fig. 6). Moreover, the maximum value of $C_{mag}(T)/R$ is higher than in the experiment. The simple NN square-lattice model is thus insufficient to describe the magnetic behavior of NaZnVOPO $_4$ (HPO $_4$). Both frustration and deformation of the square lattice affect thermodynamic properties of this compound.

D. ^{31}P NMR

NMR is a convenient local probe of both static and dynamic properties. In NaZnVOPO $_4$ (HPO $_4$), the P(1) site is strongly coupled to the V^{4+} ions within the VOP(1)O $_4$ layer, while the P(2) site which is located between the adjacent layers is weakly coupled to the V^{4+} ions [see Fig. 1(a)]. This difference allows a useful comparison and highlights the magnetic behavior of the square-lattice planes.

1. ^{31}P NMR spectra

The field-sweep ^{31}P NMR spectra above T_N measured in a radio frequency of 121 MHz are shown in Fig. 8. Each spectrum is normalized by its maximum amplitude and offset vertically by adding a constant. At high temperatures, the line is found to be narrow but asymmetric and the central peak appears at the zero-shift position. As the temperature is lowered, the line width increases drastically and becomes more anisotropic with two shoulders on either side of the central peak. This abnormal spectral shape can be attributed to two nonequivalent P sites in the crystal structure [45]. Remarkably, the complete shape of the spectra could be reproduced considering the superposition of two spectral lines [66,67]. The inset of Fig. 8 portrays the spectral fit at $T = 12$ K. We have a narrow central line with weak anisotropy and a broad asymmetric background with two distinct shoulders.

The narrow central peak shifts weakly, whereas the shoulders move significantly with decreasing temperature. Thus the narrow central line with a weak shift can be assigned to the P(2) site, which is weakly coupled, while the broad line with the strong temperature-dependent behavior corresponds to the in-plane P(1) site, which is strongly coupled to the V^{4+} spins. The asymmetric shape of both P(1) and P(2) sites is likely due to the anisotropy in $\chi(T)$ or asymmetry in the hyperfine coupling constant between the P nuclear spins and the V^{4+} electronic spins. The overall spectral shape matches exactly with the spectral shape reported for other V^{4+} -based

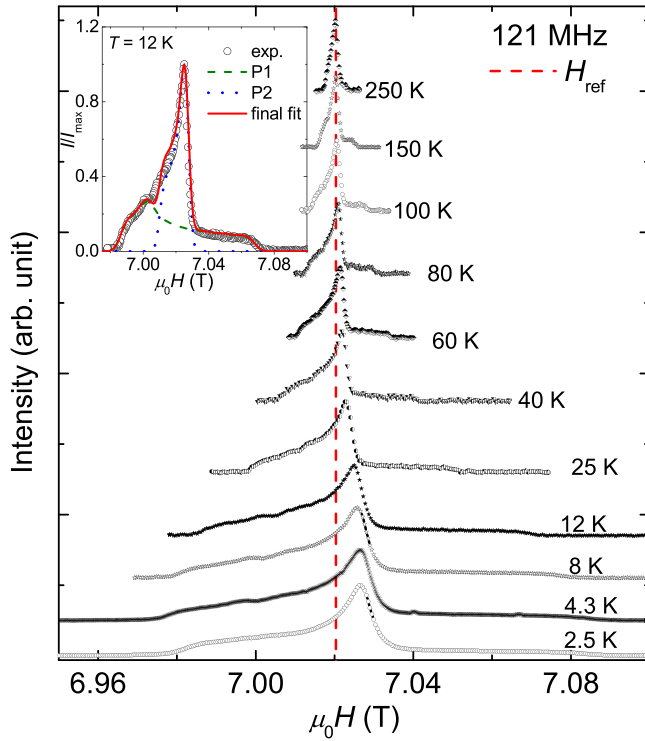


FIG. 8. Temperature evolution of the ^{31}P NMR spectra of $\text{NaZnVOPO}_4(\text{HPO}_4)$ measured at 121 MHz. The dashed line indicates the reference field position. (Inset) ^{31}P NMR spectrum at $T = 12$ K with the dashed and dotted lines are the fits of the P(1) and P(2) sites, respectively, and the solid line (final fit) is the superposition of the P(1) and P(2) fits. The NMR shift values along the x , y , and z directions, obtained from the fitting are $K_x^{(1)} \simeq 0.48\%$, $K_y^{(1)} \simeq -0.68\%$, and $K_z^{(1)} \simeq 0.24\%$ for P(1) site and $K_x^{(2)} \simeq 0.13\%$, $K_y^{(2)} \simeq -0.1\%$, and $K_z^{(2)} \simeq -0.09\%$ for P(2) site, respectively.

FSL compounds, $\text{AA}'\text{VO}(\text{PO}_4)_2$ ($\text{AA}' = \text{Pb}_2, \text{SrZn}$), on the polycrystalline sample [13,16]. The nature of the magnetic ordering can also be gleaned from the analysis of NMR spectra below T_N . Figure 9 shows the normalized ^{31}P NMR spectra measured at 121 MHz around T_N . Neither significant change in the line shape nor any visible line broadening are observed below T_N . This indicates that the ^{31}P site experiences only a weak static field in the ordered state. This observation is quite opposite to that reported for $\text{Pb}_2\text{VO}(\text{PO}_4)_2$ [13] but similar to the ^{29}Si NMR results on $\text{Li}_2\text{VOSiO}_4$ where local field on the Si site cancels out [68]. All these compounds show a similar type of magnetic layers and a similar mutual arrangement of the V^{4+} ions and PO_4/SiO_4 tetrahedra. However, only in $\text{Pb}_2\text{VO}(\text{PO}_4)_2$ the magnetic $[\text{VOPO}_4]$ layers are strongly buckled [33]. This may explain why the hyperfine couplings to V^{4+} spins with the opposite alignment do not lead to the cancellation of the local field. On the other hand, in $\text{NaZnVOPO}_4(\text{HPO}_4)$ the layers are almost flat (Fig. 1), and the absence of the ^{31}P NMR line broadening below T_N can be still ascribed to the filtering of the hyperfine fields due to the AFM spin alignments in the ground state.

2. ^{31}P NMR shift

The spectrum at each temperature was fitted following the same procedure as described above for $T = 12$ K. The

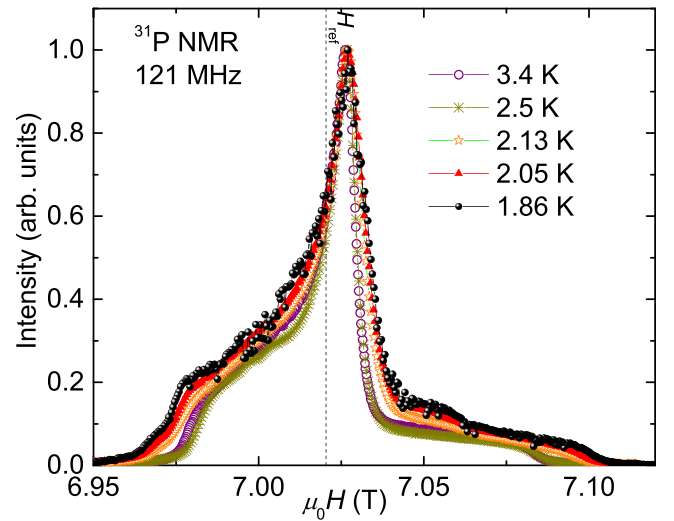


FIG. 9. Temperature-dependent ^{31}P NMR spectra of $\text{NaZnVOPO}_4(\text{HPO}_4)$ measured at 121 MHz around T_N . The dashed line indicates the reference field position.

estimated temperature-dependent NMR shift $[K(T)]$ along different orientations (K_x , K_y , and K_z) for both P(1) and P(2) sites are plotted in Figs. 10(a) and 10(b), respectively. All the components of $K(T)$ exhibit a broad maximum/minimum at around 4.3 K, an indication of the 2D AFM short-range-ordering. Further, the magnitude of $K(T)$ for the P(2) site is weaker than for the P(1) site, as expected. The isotropic NMR shift was calculated as $K_{\text{iso}} = (K_x + K_y + K_z)/3$, which is found to be almost temperature-independent for both the ^{31}P sites. This also suggests that the isotropic part of hyperfine coupling at the P site from the four neighboring V^{4+} spins is nearly averaged out.

As $K(T)$ is an intrinsic measure of the spin susceptibility $\chi_{\text{spin}}(T)$ and is free from extrinsic contributions, one can write

$$K(T) = K_0 + \frac{A_{\text{hf}}}{N_A} \chi_{\text{spin}}(T). \quad (9)$$

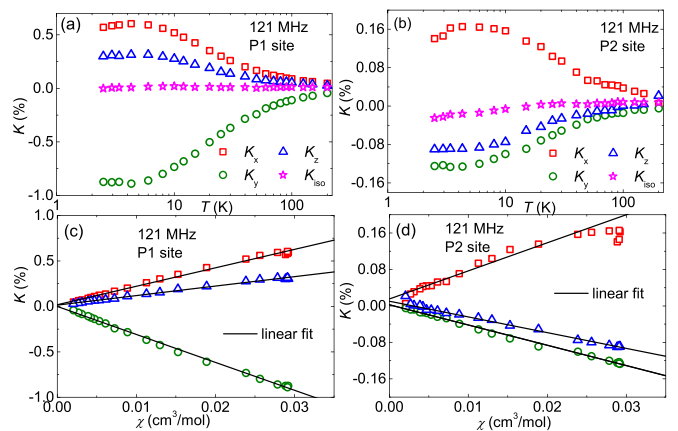


FIG. 10. Anisotropic components of K along the x , y , and z directions as a function of temperature for (a) P(1) and (b) P(2) sites, respectively. K vs χ measured at 7 T are plotted for all the three orientations for (c) P(1) and (d) P(2) sites, respectively. The solid lines are the linear fits.

Here, K_0 is the temperature-independent chemical (orbital) shift and A_{hf} is the hyperfine coupling constant between the ^{31}P nucleus and V^{4+} spins. In order to estimate A_{hf} , we have plotted K vs χ , assuming temperature as an implied variable in Figs. 10(c) and 10(d) for P(1) and P(2) sites, respectively. In every case, K vs χ plot is linear in the whole temperature range. Linear fits return $A_{\text{hf}}^{(1)} = (1134 \pm 19) \text{ Oe}/\mu_{\text{B}}$, $(-1716 \pm 20) \text{ Oe}/\mu_{\text{B}}$, and $(582.59 \pm 11) \text{ Oe}/\mu_{\text{B}}$ along the x , y , and z directions for the P(1) site and $A_{\text{hf}}^{(2)} = (343 \pm 13) \text{ Oe}/\mu_{\text{B}}$, $(-248 \pm 4) \text{ Oe}/\mu_{\text{B}}$, and $(-192 \pm 3) \text{ Oe}/\mu_{\text{B}}$ along the x , y , and z directions for the P(2) site, respectively. Clearly, the magnitude of $A_{\text{hf}}^{(1)}$ is almost one order of magnitude larger than $A_{\text{hf}}^{(2)}$ in all the three directions, thus proving the stronger coupling for P(1) than P(2).

For the P(1) site, the transferred hyperfine coupling mainly arises from the interactions with the four nearest-neighbor V^{4+} spins in the plane. The isotropic and anisotropic transferred hyperfine couplings originate from $\text{P}(3s)\text{-O}(2p)\text{-V}(3d)$ and $\text{P}(3p)\text{-O}(2p)\text{-V}(3d)$ covalent bonds, respectively. Since P(1) is surrounded by four V^{4+} ions forming a nearly square lattice in the plane, the experimentally observed asymmetry in hyperfine field indicates nonequivalent $\text{P}(3p)\text{-O}(2p)\text{-V}(3d)$ bonds for the four NN V^{4+} ions and hence a distortion in the square lattice, consistent with the low symmetry of the crystal structure as pointed out earlier.

3. Spin-lattice relaxation rate ^{31}P $1/T_1$

We have performed ^{31}P spin-lattice relaxation rate ($1/T_1$) measurements as a function of temperature down to 1.7 K at two different frequencies, 30.2 and 121 MHz. The recovery of the longitudinal nuclear magnetization after a saturation pulse could be fitted by a double exponential function

$$1 - \frac{M(t)}{M(\infty)} = Ae^{-t/T_{11}} + Be^{-t/T_{12}}, \quad (10)$$

where $M(t)$ is the nuclear magnetization at a time t after the saturation pulse and $M(\infty)$ is the equilibrium nuclear magnetization. As each NMR spectrum is a superposition of two P-sites, which are inseparable, a double exponential function is used to fit the recovery curves. In Eq. (10), $1/T_{11}$ and $1/T_{12}$ are the spin-lattice relaxation rates for P(1) and P(2) sites, respectively, and A and B account for their respective weight factors. At 121 MHz, the total spectral width was large and we were not able to saturate the whole spectrum using a single saturation pulse. Therefore $1/T_1$ is also measured at a lower frequency of 30.2 MHz where the spectral width is reduced significantly and we were able to saturate the whole spectrum above T_{N} .

The extracted $1/T_{11}$ and $1/T_{12}$ as a function of temperature at 30.2 and 121 MHz and for both the P sites are presented in Fig. 11(b). In the high-temperature ($T \geq 4.3 \text{ K}$) region, $1/T_1$ for both the P sites are almost constant, typically expected in the paramagnetic regime [69]. At low temperatures, $1/T_{11}$ and $1/T_{12}$ show sharp peaks at around $T_{\text{N}} \simeq 2.04$ and 2.36 K for 30.2 and 121 MHz, respectively, indicating the slowing down of fluctuating moments as we approach the magnetic LRO. Below T_{N} , both $1/T_{11}$ and $1/T_{12}$ decrease toward zero due to the scattering of magnons by the nuclear spins [70].

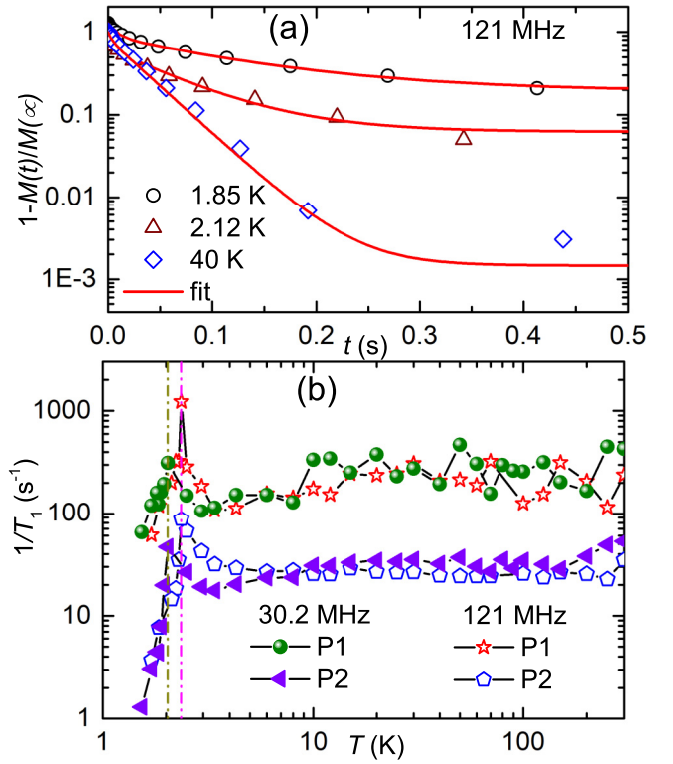


FIG. 11. (a) Longitudinal recovery curves at three selected temperatures. The solid lines are fits using Eq. (10). (b) ^{31}P spin-lattice relaxation rates for P(1) ($1/T_{11}$) and P(2) ($1/T_{12}$) sites as a function of temperature measured in 30.2 and 121 MHz. The data are shown in a log-log scale in order to highlight the peak at T_{N} . The vertical dashed-dotted lines indicate the magnetic LRO at $T_{\text{N}} \simeq 2.04$ and $\simeq 2.36 \text{ K}$ for 30.2 and 121 MHz data, respectively.

E. Microscopic magnetic model

Before discussing the magnetic model, we determine the position of hydrogen, which may be crucial for the correct evaluation of exchange couplings [71]. In hydrophosphates, one expects a deformation of PO_4 tetrahedra because one of the oxygens is linked to hydrogen and should thus weaken its bond to phosphorous in order to keep the overall bond valence unchanged. Such a deformation is observed in the $\text{P}(2)\text{O}_4$ tetrahedra with the P–O bond distances of 1.490 [O(1)], 1.530 [O(7)], 1.537 [O(2)], and 1.585 Å [O(9)] [45]. We thus considered different hydrogen positions in the vicinity of O(9) and found the lowest energy for hydrogen located at (0.7658, 0.2823, 0.7588) and separated from oxygen by 0.988 Å. The O–H bond is directed toward the $[\text{VOPO}_4]$ layer, with the H atom forming three hydrogen bonds of 2.2–2.4 Å to oxygen atoms of the VO_5 pyramids and $\text{P}(1)\text{O}_4$ tetrahedra (Fig. 1).

We now adopt this hydrogen position in DFT calculations and evaluate exchange couplings using two complementary methods. The first one is superexchange model [50] based on electron hoppings extracted from Wannier fits to the PBE band structure, resulting in

$$J_i = \frac{4t_{xy \rightarrow xy}^2}{U_{\text{eff}}} - \sum_{\alpha} \frac{4t_{xy \rightarrow \alpha}^2 J_{\text{eff}}}{(U_{\text{eff}} + \Delta_{\alpha})(U_{\text{eff}} + \Delta_{\alpha} - J_{\text{eff}})}, \quad (11)$$

TABLE I. Interatomic V-V distances (in Å) and exchange couplings (in K). The FM and AFM contributions are obtained from the superexchange model, Eq. (11), whereas total exchange couplings J_i are calculated via the DFT + U mapping procedure and thus deviate from $J_i^{\text{FM}} + J_i^{\text{AFM}}$.

	$d_{\text{V-V}}$	J_i^{AFM}	J_i^{FM}	J_i
J_1	4.616	1.4	-5.6	-5.1
J'_1	4.542	1.4	-7.4	-7.9
J''_1	4.785	2.6	-3.1	-1.0
J_2	6.380	18.7	-0.4	8.1
J'_2	6.395	9.1	-0.4	4.6

where d_{xy} is the half-filled orbital of V^{4+} , α labels unoccupied d orbitals, and Δ_α is the crystal-field splitting. The first term stands for AFM superexchange arising from electron hoppings between the half-filled orbitals, whereas the second term is FM superexchange due to electron hoppings between the half-filled and empty orbitals. Using the effective Coulomb repulsion of $U_{\text{eff}} = 4$ eV and Hund's coupling of $J_{\text{eff}} = 1$ eV¹ from Refs. [51,53], we arrive at the exchange couplings J_i^{AFM} and J_i^{FM} listed in Table I. Additionally, we compute total exchange couplings J_i via the DFT + U mapping approach [52,53].

Both methods arrive at qualitatively similar results. The NN couplings are FM, whereas the NNN couplings are AFM in nature, thus favoring solution- b for the susceptibility fits. The largest anisotropy is observed between J'_1 and J''_1 . However, on average these couplings—both running along c —differ from J_1 (along b) by 20% only. The spatial anisotropy of the NNN couplings is more significant with $J_2/J'_2 \simeq 1.8$. The overall energy scale of the NNN couplings, $\bar{J}_2 \simeq 5.6$ K, is similar to $\text{Li}_2\text{VOSiO}_4$ ($J_2 \simeq 5.9$ K [55]) and $\text{Na}_{1.5}\text{VOPO}_4\text{F}_{0.5}$ ($\bar{J}_2 \simeq 6.6$ K) and much lower than in $\text{Pb}_2\text{VO}(\text{PO}_4)_2$ with $\bar{J}_2 \simeq 9.3$ K [13] or $\text{SrZnVO}(\text{PO}_4)_2$ with $\bar{J}_2 = 8.6$ K [16]. This difference can be traced back to the buckling of the magnetic layers in $\text{AA}'\text{VO}(\text{PO}_4)_2$ ($\text{AA}' = \text{Pb}_2, \text{SrZn}$), while the layers are almost or even perfectly flat in $\text{NaZnVOPO}_4(\text{HPO}_4)$ (Fig. 1), $\text{Li}_2\text{VOSiO}_4$, and $\text{Na}_{1.5}\text{VOPO}_4\text{F}_{0.5}$.

IV. DISCUSSION

Our data suggest that $\text{NaZnVOPO}_4(\text{HPO}_4)$ is well described by the spin-1/2 FSL model if deformation of the square lattice is taken into account. Although individual data sets such as field-dependent magnetization may be consistent even with a nonfrustrated square lattice, the reduced size of the specific heat maximum, $C_{\text{max}}^{\text{mag}}/R \simeq 0.41$, indicates the presence of frustration. Indeed, the value of the frustration parameter $f = \frac{|\theta_{\text{CW}}|}{T_N} \simeq 2.1$ reflects a moderate frustration in the compound. The value of $\alpha = \bar{J}_2/\bar{J}_1 \simeq -4.3$ (with $\bar{J}_1 \simeq -1.3$ K, $\bar{J}_2 \simeq 5.6$ K) locates this compound in the CAF regime of the J_1 - J_2 phase diagram.

¹Note that U_{eff} and J_{eff} apply to V-based Wannier functions that include both V $3d$ and O $2p$ orbitals, while the DFT + U parameters U_d and J_d mentioned in Sec. II describe, respectively, the Coulomb repulsion and Hund's coupling in V $3d$ orbitals only.

In a spin system, the spin-lattice relaxation rate carries information on the low-lying excitations or spin dynamics in the momentum space. Typically, $\frac{1}{T_1 T}$ can be expressed in terms of the dynamic susceptibility $\chi_M(\vec{q}, \omega_0)$ as [72]

$$\frac{1}{T_1 T} = \frac{2\gamma_N^2 k_B}{N_A^2} \sum_{\vec{q}} |A(\vec{q})|^2 \frac{\chi_M''(\vec{q}, \omega_0)}{\omega_0}, \quad (12)$$

where the sum is over the wave vector \vec{q} within the first Brillouin zone, $A(\vec{q})$ is the form-factor of the hyperfine interaction, and $\chi_M''(\vec{q}, \omega_0)$ is the imaginary part of the dynamic susceptibility at the nuclear Larmor frequency ω_0 . The dominance of different q components [$\vec{q} = 0$ and $\vec{q} = (\pm\pi/a, \pm\pi/b)$] is often visible in the $1/T_1$ data when plotted against temperature, especially for the low-dimensional spin systems with strong exchange coupling. At very high temperatures ($T > J/k_B$), $1/T_1$ is almost temperature-independent due to uncorrelated moments and can be expressed as [13]

$$\left(\frac{1}{T_1}\right)_{T \rightarrow \infty} = \frac{(\gamma_N g \mu_B)^2 \sqrt{2\pi} z' S(S+1)}{3\omega_{\text{ex}}} \times \frac{\left(\frac{A_x}{z'}\right)^2 + \left(\frac{A_y}{z'}\right)^2 + \left(\frac{A_z}{z'}\right)^2}{3}, \quad (13)$$

where $\omega_{\text{ex}} = [\max(|J_1|, |J_2|)k_B/\hbar]\sqrt{\frac{2z'S(S+1)}{3}}$ is the Heisenberg exchange frequency, z is the number of NN spins of each V^{4+} ion, and z' is the number of NN V^{4+} spins of the P(1) site. In the above expression, the hyperfine couplings along different directions are divided by z' in order to account for the coupling of P site with the individual V^{4+} ion. As the measurements are carried out on the powder sample, we have taken the rms average of the couplings along three directions.

For a tentative estimation of the in-plane exchange coupling between the V^{4+} ions we took the high-temperature value of $1/T_{11}$ for the strongly coupled P(1) site. Using the experimental parameters obtained for this site ($A_x^1 \simeq 1134$ Oe/ μ_B , $A_y^1 \simeq -1716$ Oe/ μ_B , $A_z^1 \simeq 582$ Oe/ μ_B , $\gamma_N = 108.303 \times 10^2$ rad sec⁻¹/Oe, $z' = 4$, $z = 4$, $g = 2.04$, $S = 1/2$, and $1/T_{11} \simeq 150$ sec⁻¹), the magnitude of the maximum exchange coupling strength between V^{4+} ions is estimated to be $\max(|J_1|, |J_2|) \simeq 4.2$ K. This value is indeed very close to the dominant in-plane AFM exchange coupling for both the solutions (a and b), obtained from the $\chi(T)$ analysis.

It is also instructive to compare the transition temperatures of V^{4+} -based FSL magnets. $\text{NaZnVOPO}_4(\text{HPO}_4)$ and $\text{Li}_2\text{VOSiO}_4$ feature almost the same $\bar{J}_2 \simeq 6$ K but different signs of J_1 (FM and AFM, respectively), while the former compound has a much lower $T_N \simeq 2.1$ K than the latter ($T_N \simeq 2.8$ K [11]). This indicates that FM couplings J_1 together with the deformation of the square lattice lead to a visible reduction in T_N in $\text{NaZnVOPO}_4(\text{HPO}_4)$. On the other hand, $\text{Pb}_2\text{VO}(\text{PO}_4)_2$ shows an even higher $T_N \simeq 3.65$ K [13] because of the 30% increase in the magnitude of \bar{J}_2 . This comparison illustrates that buckling of the $[\text{VOPO}_4]$ layers caused

by variable spacers between the magnetic layers effectively tunes magnetic interactions in FSL-like compounds.

V. SUMMARY

We have studied the magnetism of $\text{NaZnVOPO}_4(\text{HPO}_4)$ using wide variety of experimental techniques and complementary *ab initio* calculations. The unit cell volume as a function of T could be fitted well using the Debye model with $\theta_D \simeq 312$ K. From thermodynamic measurements we infer that the ideal FSL model captures all main features of the $\text{NaZnVOPO}_4(\text{HPO}_4)$ magnetism. However, including the spatial anisotropy of nearest-neighbor couplings is essential to reproduce the experimental saturation field. The reduced maximum of the magnetic specific heat further signals this spatial anisotropy, whereas asymmetric hyperfine couplings of the ^{31}P nuclei with the V^{4+} spins provide a direct experimental evidence for the deformation of the frustrated square lattice.

The averaged exchange couplings extracted from the magnetic susceptibility and specific heat data are $\bar{J}_1 \simeq -1.3$ K and $\bar{J}_2 \simeq 5.6$ K, resulting in the effective frustration ratio $\alpha \simeq -4.3$. Consequently, the magnetic LRO transition observed

at $T_N \simeq 2.1$ K is expected to lead to the CAF type order. A slightly larger value of f (>1) further implies moderate frustration in the spin system.

With almost flat magnetic layers, $\text{NaZnVOPO}_4(\text{HPO}_4)$ shows weaker next-nearest-neighbor couplings (\bar{J}_2) than other V^{4+} phosphates. This reduction in \bar{J}_2 along with the deformation of the square lattice lead to a lower magnetic transition temperature than in most of the other FSL candidates.

ACKNOWLEDGMENTS

S.G. and R.N. would like to acknowledge SERB, India for financial support bearing sanction Grant No. CRG/2019/000960. S.G. is supported by the Prime Ministers Research Fellowship (PMRF) scheme, Government of India. We also acknowledge the support of the HLD at HZDR, member of European Magnetic Field Laboratory (EMFL). Work at the Ames Laboratory was supported by the U.S. Department of Energy, Office of Science, Basic Energy Sciences, Materials Sciences and Engineering Division. The Ames Laboratory is operated for the U.S. Department of Energy by Iowa State University under Contract No. DEAC02-07CH11358.

-
- [1] L. Savary and L. Balents, Quantum spin liquids: a review, *Rep. Prog. Phys.* **80**, 016502 (2017); L. Balents, Spin liquids in frustrated magnets, *Nature (London)* **464**, 199 (2010).
- [2] N. Shannon, B. Schmidt, K. Penc, and P. Thalmeier, Finite temperature properties and frustrated ferromagnetism in a square lattice Heisenberg model, *Eur. Phys. J. B* **38**, 599 (2004).
- [3] B. Schmidt and P. Thalmeier, Néel temperature and reentrant H - T phase diagram of quasi-two-dimensional frustrated magnets, *Phys. Rev. B* **96**, 214443 (2017).
- [4] G.-M. Zhang, H. Hu, and L. Yu, Valence-Bond Spin-Liquid State in Two-Dimensional Frustrated Spin-1/2 Heisenberg Antiferromagnets, *Phys. Rev. Lett.* **91**, 067201 (2003).
- [5] W.-J. Hu, F. Becca, A. Parola, and S. Sorella, Direct evidence for a gapless Z_2 spin liquid by frustrating Néel antiferromagnetism, *Phys. Rev. B* **88**, 060402(R) (2013).
- [6] L. Wang and A. W. Sandvik, Critical Level Crossings and Gapless Spin Liquid in the Square-Lattice Spin-1/2 $J_1 - J_2$ Heisenberg Antiferromagnet, *Phys. Rev. Lett.* **121**, 107202 (2018).
- [7] S.-S. Gong, W. Zhu, D. N. Sheng, O. I. Motrunich, and M. P. A. Fisher, Plaquette Ordered Phase and Quantum Phase Diagram in the Spin-1/2 J_1 - J_2 Square Heisenberg Model, *Phys. Rev. Lett.* **113**, 027201 (2014).
- [8] R. L. Doretto, Plaquette valence-bond solid in the square-lattice J_1 - J_2 antiferromagnet Heisenberg model: A bond operator approach, *Phys. Rev. B* **89**, 104415 (2014).
- [9] R. Haghshenas and D. N. Sheng, U(1)-symmetric infinite projected entangled-pair states study of the spin-1/2 square J_1 - J_2 Heisenberg model, *Phys. Rev. B* **97**, 174408 (2018).
- [10] N. Shannon, T. Momoi, and P. Sindzingre, Nematic Order in Square Lattice Frustrated Ferromagnets, *Phys. Rev. Lett.* **96**, 027213 (2006).
- [11] R. Melzi, P. Carretta, A. Lascialfari, M. Mambrini, M. Troyer, P. Millet, and F. Mila, $\text{Li}_2\text{VO}(\text{Si}, \text{Ge})\text{O}_4$, a Prototype of a Two-Dimensional Frustrated Quantum Heisenberg Antiferromagnet, *Phys. Rev. Lett.* **85**, 1318 (2000).
- [12] H. Rosner, R. P. Singh, W. H. Zheng, J. Oitmaa, S.-L. Drechsler, and W. E. Pickett, Realization of a large J_2 quasi-2D spin-half Heisenberg system: $\text{Li}_2\text{VOSiO}_4$, *Phys. Rev. Lett.* **88**, 186405 (2002).
- [13] R. Nath, Y. Furukawa, F. Borsa, E. E. Kaul, M. Baenitz, C. Geibel, and D. C. Johnston, Single-crystal ^{31}P NMR studies of the frustrated square-lattice compound $\text{Pb}_2\text{VO}(\text{PO}_4)_2$, *Phys. Rev. B* **80**, 214430 (2009).
- [14] B. Roy, Y. Furukawa, R. Nath, and D. C. Johnston, Low-temperature ^{31}P NMR study of the two-dimensional frustrated square lattice compound $\text{BaCdVO}(\text{PO}_4)_2$, *J. Phys.: Conf. Ser.* **320**, 012048 (2011).
- [15] A. A. Tsirlin, R. Nath, A. M. Abakumov, R. V. Shpanchenko, C. Geibel, and H. Rosner, Frustrated square lattice with spatial anisotropy: Crystal structure and magnetic properties of $\text{PbZnVO}(\text{PO}_4)_2$, *Phys. Rev. B* **81**, 174424 (2010).
- [16] L. Bossoni, P. Carretta, R. Nath, M. Moscardini, M. Baenitz, and C. Geibel, NMR and μSR study of spin correlations in $\text{SrZnVO}(\text{PO}_4)_2$: An $S = 1/2$ frustrated magnet on a square lattice, *Phys. Rev. B* **83**, 014412 (2011).
- [17] A. A. Tsirlin, R. Nath, A. M. Abakumov, Y. Furukawa, D. C. Johnston, M. Hemmida, H.-A. Krug von Nidda, A. Loidl, C. Geibel, and H. Rosner, Phase separation and frustrated square lattice magnetism of $\text{Na}_{1.5}\text{VOPO}_4\text{F}_{0.5}$, *Phys. Rev. B* **84**, 014429 (2011).
- [18] R. Nath, A. A. Tsirlin, H. Rosner, and C. Geibel, Magnetic properties of $\text{BaCdVO}(\text{PO}_4)_2$: A strongly frustrated spin-1/2 square lattice close to the quantum critical regime, *Phys. Rev. B* **78**, 064422 (2008).
- [19] A. Yogi, N. Ahmed, R. Nath, A. A. Tsirlin, S. Kundu, A. V. Mahajan, J. Sichelschmidt, B. Roy, and Y. Furukawa,

- Antiferromagnetism of $\text{Zn}_2\text{VO}(\text{PO}_4)_2$ and the dilution with Ti^{4+} , *Phys. Rev. B* **91**, 024413 (2015).
- [20] A. Kiani and E. Pavarini, Electronic correlation and magnetic frustration in $\text{Li}_2\text{VOSiO}_4$ and VOMoO_4 , *Phys. Rev. B* **94**, 075112 (2016).
- [21] A. Bombardi, L. C. Chapon, I. Margiolaki, C. Mazzoli, S. Gonthier, F. Duc, and P. G. Radaelli, Magnetic order and lattice anomalies in the $J_1 - J_2$ model system VOMoO_4 , *Phys. Rev. B* **71**, 220406(R) (2005).
- [22] P. Carretta, N. Papinutto, C. B. Azzoni, M. C. Mozzati, E. Pavarini, S. Gonthier, and P. Millet, Frustration-driven structural distortion in VOMoO_4 , *Phys. Rev. B* **66**, 094420 (2002).
- [23] A. A. Tsirlin, A. A. Belik, R. V. Shpanchenko, E. V. Antipov, E. Takayama-Muromachi, and H. Rosner, Frustrated spin-1/2 square lattice in the layered perovskite PbVO_3 , *Phys. Rev. B* **77**, 092402 (2008).
- [24] H. Ishikawa, N. Nakamura, M. Yoshida, M. Takigawa, P. Babkevich, N. Qureshi, H. M. Rønnow, T. Yajima, and Z. Hiroi, $J_1 - J_2$ square-lattice Heisenberg antiferromagnets with $4d^1$ spins: AMoOPO_4Cl ($A = \text{K, Rb}$), *Phys. Rev. B* **95**, 064408 (2017).
- [25] H. Takeda, T. Yamauchi, M. Takigawa, H. Ishikawa, and Z. Hiroi, Pressure-induced phase transition in the J_1 - J_2 square lattice antiferromagnet $\text{RbMoOPO}_4\text{Cl}$, *Phys. Rev. B* **103**, 104406 (2021).
- [26] Y. Xu, S. Liu, N. Qu, Y. Cui, Q. Gao, R. Chen, J. Wang, F. Gao, and X. Hao, Comparative description of magnetic interactions in $\text{Sr}_2\text{CuTeO}_6$ and Sr_2CuWO_6 , *J. Phys.: Condens. Matter* **29**, 105801 (2017).
- [27] S. Vasala, M. Avdeev, S. Danilkin, O. Chmaissem, and M. Karppinen, Magnetic structure of Sr_2CuWO_6 , *J. Phys.: Condens. Matter* **26**, 496001 (2014).
- [28] T. Koga, N. Kurita, M. Avdeev, S. Danilkin, T. J. Sato, and H. Tanaka, Magnetic structure of the $S = 1/2$ quasi-two-dimensional square-lattice Heisenberg antiferromagnet $\text{Sr}_2\text{CuTeO}_6$, *Phys. Rev. B* **93**, 054426 (2016).
- [29] P. Babkevich, V. M. Katukuri, B. Fåk, S. Rols, T. Fennell, D. Pajić, H. Tanaka, T. Pardini, R. R. P. Singh, A. Mitrushchenkov, O. V. Yazyev, and H. M. Rønnow, Magnetic Excitations and Electronic Interactions in $\text{Sr}_2\text{CuTeO}_6$: A Spin-1/2 Square Lattice Heisenberg Antiferromagnet, *Phys. Rev. Lett.* **117**, 237203 (2016).
- [30] H. C. Walker, O. Mustonen, S. Vasala, D. J. Voneshen, M. D. Le, D. T. Adroja, and M. Karppinen, Spin wave excitations in the tetragonal double perovskite Sr_2CuWO_6 , *Phys. Rev. B* **94**, 064411 (2016).
- [31] M. Watanabe, N. Kurita, H. Tanaka, W. Ueno, K. Matsui, T. Goto, and M. Hagihala, Contrasting magnetic structures in SrLaCuSbO_6 and SrLaCuNbO_6 : Spin-1/2 quasi-square-lattice J_1 - J_2 Heisenberg antiferromagnets, *Phys. Rev. B* **105**, 054414 (2022).
- [32] S. Guchhait, S. Baby, M. Padmanabhan, A. Medhi, and R. Nath, Quasi-two-dimensional magnetism in spin-1/2 square lattice compound $\text{Cu}[\text{C}_6\text{H}_2(\text{COO})_4][\text{H}_3\text{N}(\text{CH}_2)_2\text{-NH}_3] \cdot 3\text{H}_2\text{O}$, *Europhys. Lett.* **133**, 57006 (2021).
- [33] A. A. Tsirlin and H. Rosner, Extension of the spin-1/2 frustrated square lattice model: The case of layered vanadium phosphates, *Phys. Rev. B* **79**, 214417 (2009).
- [34] S. Bettler, F. Landolt, O. M. Aksoy, Z. Yan, S. Gvasaliya, Y. Qiu, E. Ressouche, K. Beauvois, S. Raymond, A. N. Ponomaryov, S. A. Zvyagin, and A. Zheludev, Magnetic structure and spin waves in the frustrated ferro-antiferromagnet $\text{Pb}_2\text{VO}(\text{PO}_4)_2$, *Phys. Rev. B* **99**, 184437 (2019).
- [35] F. Landolt, Z. Yan, S. Gvasaliya, K. Beauvois, E. Ressouche, J. Xu, and A. Zheludev, Phase diagram and spin waves in the frustrated ferro-antiferromagnet $\text{SrZnVO}(\text{PO}_4)_2$, *Phys. Rev. B* **104**, 224435 (2021).
- [36] V. K. Bhartiya, S. Hayashida, K. Y. Povarov, Z. Yan, Y. Qiu, S. Raymond, and A. Zheludev, Inelastic neutron scattering determination of the spin hamiltonian for $\text{BaCdVO}(\text{PO}_4)_2$, *Phys. Rev. B* **103**, 144402 (2021).
- [37] K. Y. Povarov, V. K. Bhartiya, Z. Yan, and A. Zheludev, Thermodynamics of a frustrated quantum magnet on a square lattice, *Phys. Rev. B* **99**, 024413 (2019).
- [38] V. K. Bhartiya, K. Y. Povarov, D. Blosser, S. Bettler, Z. Yan, S. Gvasaliya, S. Raymond, E. Ressouche, K. Beauvois, J. Xu, F. Yokaichiya, and A. Zheludev, Presaturation phase with no dipolar order in a quantum ferro-antiferromagnet, *Phys. Rev. Research* **1**, 033078 (2019).
- [39] M. Skoulatos, F. Rucker, G. J. Nilsen, A. Bertin, E. Pomjakushina, J. Ollivier, A. Schneidewind, R. Georgii, O. Zaharko, L. Keller, C. Rüegg, C. Pfleiderer, B. Schmidt, N. Shannon, A. Kriele, A. Senyshyn, and A. Smerald, Putative spin-nematic phase in $\text{BaCdVO}(\text{PO}_4)_2$, *Phys. Rev. B* **100**, 014405 (2019).
- [40] F. Landolt, S. Bettler, Z. Yan, S. Gvasaliya, A. Zheludev, S. Mishra, I. Sheikin, S. Krämer, M. Horvatić, A. Gazizulina, and O. Prokhnenko, Presaturation phase in the frustrated ferro-antiferromagnet $\text{Pb}_2\text{VO}(\text{PO}_4)_2$, *Phys. Rev. B* **102**, 094414 (2020).
- [41] K. M. Ranjith, F. Landolt, S. Raymond, A. Zheludev, and M. Horvatić, NMR evidence against a spin-nematic nature of the presaturation phase in the frustrated magnet $\text{SrZnVO}(\text{PO}_4)_2$, *Phys. Rev. B* **105**, 134429 (2022).
- [42] F. Landolt, K. Povarov, Z. Yan, S. Gvasaliya, E. Ressouche, S. Raymond, V. O. Garlea, and A. Zheludev, Spin correlations in the frustrated ferro-antiferromagnet $\text{SrZnVO}(\text{PO}_4)_2$ near saturation, arXiv preprint [arXiv:2204.08778](https://arxiv.org/abs/2204.08778) (2022).
- [43] K. Momma and F. Izumi, VESTA 3 for three-dimensional visualization of crystal, volumetric and morphology data, *J. Appl. Crystallogr.* **44**, 1272 (2011).
- [44] J. Rodríguez-Carvajal, Recent advances in magnetic structure determination by neutron powder diffraction, *Phys. B: Condens. Matter* **192**, 55 (1993).
- [45] E. Le Fur, Y. Moreno, and J. Pivan, On the new oxovanadium phosphate $\text{NaZnVOPO}_4(\text{HPO}_4)$ obtained at 510 K from hydrothermal treatment, *J. Mater. Chem.* **11**, 1735 (2001).
- [46] Y. Skourski, M. D. Kuz'min, K. P. Skokov, A. V. Andreev, and J. Wosnitzer, High-field magnetization of $\text{Ho}_2\text{Fe}_{17}$, *Phys. Rev. B* **83**, 214420 (2011).
- [47] A. A. Tsirlin, B. Schmidt, Y. Skourski, R. Nath, C. Geibel, and H. Rosner, Exploring the spin-1/2 frustrated square lattice model with high-field magnetization studies, *Phys. Rev. B* **80**, 132407 (2009).
- [48] K. Koepernik and H. Eschrig, Full-potential nonorthogonal local-orbital minimum-basis band-structure scheme, *Phys. Rev. B* **59**, 1743 (1999).

- [49] J. P. Perdew, K. Burke, and M. Ernzerhof, Generalized Gradient Approximation Made Simple, *Phys. Rev. Lett.* **77**, 3865 (1996).
- [50] V. V. Mazurenko, F. Mila, and V. I. Anisimov, Electronic structure and exchange interactions of $\text{Na}_2\text{V}_3\text{O}_7$, *Phys. Rev. B* **73**, 014418 (2006).
- [51] A. A. Tsirlin, O. Janson, and H. Rosner, Unusual ferromagnetic superexchange in CdVO_3 : The role of Cd, *Phys. Rev. B* **84**, 144429 (2011).
- [52] H. J. Xiang, E. J. Kan, S.-H. Wei, M.-H. Whangbo, and X. G. Gong, Predicting the spin-lattice order of frustrated systems from first principles, *Phys. Rev. B* **84**, 224429 (2011).
- [53] A. A. Tsirlin, Spin-chain magnetism and uniform Dzyaloshinsky-Moriya anisotropy in BaV_3O_8 , *Phys. Rev. B* **89**, 014405 (2014).
- [54] F. Weickert, N. Harrison, B. L. Scott, M. Jaime, A. Leitm ae, I. Heinmaa, R. Stern, O. Janson, H. Berger, H. Rosner, and A. A. Tsirlin, Magnetic anisotropy in the frustrated spin-chain compound $\beta\text{-TeVO}_4$, *Phys. Rev. B* **94**, 064403 (2016).
- [55] H. Rosner, R. R. P. Singh, W. H. Zheng, J. Oitmaa, and W. E. Pickett, High-temperature expansions for the $J_1 - J_2$ Heisenberg models: Applications to ab initio calculated models for $\text{Li}_2\text{VOSiO}_4$ and $\text{Li}_2\text{VOGeO}_4$, *Phys. Rev. B* **67**, 014416 (2003).
- [56] F. Alet, S. Wessel, and M. Troyer, Generalized directed loop method for quantum monte carlo simulations, *Phys. Rev. E* **71**, 036706 (2005).
- [57] A. W. Sandvik, Stochastic series expansion method with operator-loop update, *Phys. Rev. B* **59**, R14157 (1999).
- [58] B. Bauer, L. D. Carr, H. G. Evertz, A. Feiguin, J. Freire, S. Fuchs, L. Gamper, J. Gukelberger, E. Gull, S. Guertler *et al.*, The ALPS project release 2.0: open source software for strongly correlated systems, *J. Stat. Mech.: Theory Exp.* (2011) P05001.
- [59] D. C. Wallace, *Thermodynamics of Crystals* (Dover Publications, New York, 1998).
- [60] L. E. Budd, R. M. Ibberson, W. G. Marshall, and S. Parsons, The effect of temperature and pressure on the crystal structure of piperidine, *Chemistry Central Journal* **9**, 18 (2015); S. Guchhait, Q.-P. Ding, M. Sahoo, A. Giri, S. Maji, Y. Furukawa, and R. Nath, Quasi-one-dimensional uniform spin-1/2 Heisenberg antiferromagnet $\text{KNaCuP}_2\text{O}_7$ probed by ^{31}P and ^{23}Na NMR, *Phys. Rev. B* **103**, 224415 (2021).
- [61] C. Kittel, *Introduction to Solid State Physics*, 8th ed. (Wiley, New York, 2004).
- [62] P. W. Selwood, *Magnetochemistry* (Read Books Ltd., Redditch, UK, 2013).
- [63] P. K. Mukharjee, K. M. Ranjith, M. Baenitz, Y. Skourski, A. A. Tsirlin, and R. Nath, Two types of alternating spin-1/2 chains and their field-induced transitions in $\epsilon\text{-LiVOPO}_4$, *Phys. Rev. B* **101**, 224403 (2020).
- [64] P. Thalmeier, M. E. Zhitomirsky, B. Schmidt, and N. Shannon, Quantum effects in magnetization of $J_1\text{-}J_2$ square lattice antiferromagnet, *Phys. Rev. B* **77**, 104441 (2008).
- [65] S. J. Sebastian, K. Somesh, M. Nandi, N. Ahmed, P. Bag, M. Baenitz, B. Koo, J. Sichelschmidt, A. A. Tsirlin, Y. Furukawa, and R. Nath, Quasi-one-dimensional magnetism in the spin-1/2 antiferromagnet $\text{BaNa}_2\text{Cu}(\text{VO}_4)_2$, *Phys. Rev. B* **103**, 064413 (2021).
- [66] P. K. Mukharjee, K. Somesh, K. M. Ranjith, M. Baenitz, Y. Skourski, D. T. Adroja, D. Khalyavin, A. A. Tsirlin, and R. Nath, Quantum magnetism of ferromagnetic spin dimers in $\alpha\text{-KVOPO}_4$, *Phys. Rev. B* **104**, 224409 (2021).
- [67] C. P. Slichter, *Principle of Nuclear Magnetic Resonance*, 3rd ed. (Springer, New York, 1996).
- [68] R. Melzi, S. Aldrovandi, F. Tedoldi, P. Carretta, P. Millet, and F. Mila, Magnetic and thermodynamic properties of $\text{Li}_2\text{VOSiO}_4$: A two-dimensional $S = 1/2$ frustrated antiferromagnet on a square lattice, *Phys. Rev. B* **64**, 024409 (2001).
- [69] T. Moriya, Nuclear magnetic relaxation in antiferromagnetics, *Prog. Theor. Phys.* **16**, 23 (1956).
- [70] S. S. Islam, K. M. Ranjith, M. Baenitz, Y. Skourski, A. A. Tsirlin, and R. Nath, Frustration of square cupola in $\text{Sr}(\text{TiO})\text{Cu}_4(\text{PO}_4)_4$, *Phys. Rev. B* **97**, 174432 (2018).
- [71] S. Lebernegg, A. A. Tsirlin, O. Janson, and H. Rosner, Two energy scales of spin dimers in clinoclase $\text{Cu}_3(\text{AsO}_4)(\text{OH})_3$, *Phys. Rev. B* **87**, 235117 (2013).
- [72] T. Moriya, The effect of electron-electron interaction on the nuclear spin relaxation in metals, *J. Phys. Soc. Jpn.* **18**, 516 (1963).